Check for updates

A kernel-based machine learning potential and quantum vibrational state analysis of the cationic Ar hydride (Ar$_2$H$^+$)†

María Judit Montes de Oca-Estévez, [iD] ‡[ab] Álvaro Valdés [iD] [c] and Rita Prosmiti [iD] *[a]

One of the most fascinating discoveries in recent years, in the cold and low pressure regions of the universe, was the detection of ArH$^+$ and HeH$^+$ species. The identification of such noble gas-containing molecules in space is the key to understanding noble gas chemistry. In the present work, we discuss the possibility of [Ar$_2$H]$^+$ existence as a potentially detectable molecule in the interstellar medium, providing new data on possible astronomical pathways and energetics of this compound. As a first step, a data-driven approach is proposed to construct a full 3D machine-learning potential energy surface (ML-PES) *via* the reproducing kernel Hilbert space (RKHS) method. The training and testing data sets are generated from CCSD(T)/CBS[56] computations, while a validation protocol is introduced to ensure the quality of the potential. In turn, the resulting ML-PES is employed to compute vibrational levels and molecular spectroscopic constants for the cation. In this way, the most common isotopologue in ISM, [^{36}Ar$_2$H]$^+$, was characterized for the first time, while simultaneously, comparisons with previously reported values available for [^{40}Ar$_2$H]$^+$ are discussed. Our present data could serve as a benchmark for future studies on this system, as well as on higher-order cationic Ar-hydrides of astrophysical interest.

The recorded presence of the simplest noble gas hydride cations, HeH^{+1} and ArH$^+$,^{2,3} in interstellar medium (ISM) has revolutionised gas-phase ion chemistry. The closed shell structure of noble gas (Ng) atoms is responsible for these species being known to be chemically inert with a limited ability to interact with other molecular systems or atoms through extraordinarily weak van der Waals (vdW) forces. This claim is definitely true for neutral systems, however, the recent discoveries of argonium and helonium has confirmed that with the appropriate ligands, and under specific conditions of temperature and pressure, these species are capable of forming strong covalent bonds.$^{4–9}$ In this way, our perception of noble gas molecules changes, expanding our knowledge about these systems and opening up new possibilities in the field of astrochemistry.

For all these reasons, it is not surprising that, in recent years, there has been a revival of interest in noble gas hydride cations [Ng$_n$H$_m$]$^+$ (n, m > 1) in order to employ the advances in computational quantum chemistry and experimental laboratory techniques, to help understand the chemical nature of these compounds and their evolution in the ISM. The first spectroscopic evidence for the existence of [Ng$_n$H]$^+$ complexes dates back to 1972, when Bondybey and Pimentel^{10} recorded absorption bands at 905/644 and 852/607 cm^{-1} in the infrared spectra of inert gas-hydrogen matrix samples, corresponding to Ar–H$_2^+$/D$_2^+$ and Kr–H$_2^+$/D$_2^+$, respectively. Later studies along this line$^{11–14}$ reassigned the bands to Ar$_n$H$^+$ and Ar$_n$D$^+$ structures without establishing the number of noble gas atoms present in the systems, and finally, Friedgen and Parnis^{15} through electron bombardment matrix isolation of Ng/Ng/methanol mixtures (Ng = Ar, Kr and Xe) revealed, among others features of proton-bound dimers, a peak at 903.8 cm^{-1} corresponding to the [Ar$_2$H]$^+$ complex. More recently, Ar$_n$H$^+$ complexes have also been produced in pulsed-discharge supersonic expansions containing hydrogen and argon,^{16} and species with n = 3–7 have been characterized by infrared laser photodissociation spectroscopy, reporting measurements for different vibrational fundamental and combination band frequencies.

Simultaneously, [Ng$_2$H]$^+$ cations have been investigated theoretically, in order to understand their electronic structures and bonding.$^{14,16–32}$ One of the first studies by Lundell *et al.*,^{18} analyzed the molecular properties of the proton-bound dimers using *ab initio* methods with both the effective core potentials

^{a} *Institute of Fundamental Physics (IFF-CSIC), CSIC, Serrano 123, 28006 Madrid, Spain. E-mail: rita@iff.csic.es; Tel: +34 915616800*

^{b} *Atelgraphics S.L., Mota de Cuervo 42, 28043, Madrid, Spain*

^{c} *Escuela de Física, Universidad Nacional de Colombia, Sede Medellín, A. A., 3840, Medellín, Colombia*

† Electronic supplementary information (ESI) available. See DOI: https://doi.org/10.1039/d3cp05865d

‡ Doctoral Programme in Theoretical Chemistry and Computational Modelling, Doctoral School, Universidad Autónoma de Madrid, Spain.

7060 | *Phys. Chem. Chem. Phys.*, 2024, **26**, 7060–7071

This journal is © the Owner Societies 2024

and all electron basis sets. In general, the Ng_2H^+ (Ng = Ar, Kr, Xe) molecules were found to have a linear symmetric center $D_{\infty h}$ geometry. Although the first calculations for the Ar_2H^+ predicted unequal Ar–H bonds,[18] the centrosymmetric $[Ar_2H]^+$ structure was later confirmed.[19] Therefore, more extensive investigations were performed on protonated rare gas homo/hetero-dimers in order to determine the spectroscopic properties and binding energies employing *ab initio* high level of theory methodologies.[25,26]

Our previous studies showed that $ArH^{+8,9}$ is an inflexion point in the behaviors of the NgH^+ systems. Moreover, one should also add the singularity associated with the isotopes of Ar in ISM, which makes it a very attractive objective for the investigations. The Ar atom has three stable isotopes: ^{36}Ar, ^{38}Ar and ^{40}Ar. In the Earth's atmosphere, Ar constitutes 0.94% of all the elements that compose the mass of dry air, being the third most abundant element. ^{40}Ar is the most abundant isotope with a ratio 1584 with respect to its homologues $^{36/38}Ar$ (1.00/5.30).[33] Notwithstanding, ^{36}Ar is the most common isotope in the ISM (84.6%), followed by ^{38}Ar (15.4%) and traces of ^{40}Ar (0.025%).[34]

Therefore, the complex formed by the addition of a new Ar atom to the simplest argon hydride cation, is proposed as a potentially detectable candidate in the ISM. The lack of dipole moment of this protonated Ar-dimer makes it impossible to observe through rotational spectroscopy. For this reason, its presence in the universe has to be confirmed using vibrational spectroscopy, or by rotation of the excited vibrational levels. In this way, some theoretical investigations have already been carried out to determine the vibrational spectrum of this molecule, and for that, it is essential to determine an accurate global potential energy surface (PES) for the Ar_2H^+ system. There are few studies in which force-fields or full-PES (based on traditional fitting methods) have been generated for $[Ar_2H]^+$. Among them, the earliest PES is that constructed by Qu *et al.*[22] from QCISD/6-311++G(3df,3pd) *ab initio* calculations considering up to three-body terms in the potential expansion. Subsequently, Fortenberry[25] reported quartic force-fields from CCSD(T)/CBS[TQ5], core-correlation and relativistic computations, while Tan *et al.*[28] employed a Gaussian quadrature equally-spaced grid of 3000 CCSD(T)/aug-cc-pVQZ//MP2/aug-cc-pVQZ points to build the PES. The most recent analytical 3D PES reported by Koner[29] has been expressed in two-body (both short and long-range parts), and three-body terms, which have been parameterized to diatomic and triatomic CCSD(T)/aug-cc-pVQZ interaction energies, respectively, with the asymptotic behavior represented by a standard long-range expansion form for the diatomic potentials.

On the one hand, conventional fitting processes have been demonstrated that can provide high quality PESs,[35–42] nevertheless, constructing such analytical representations of the PES can be a tedious and considerably time-consuming task. On the other hand, even in the case of a 3D molecular system, where high level quantum mechanical calculations are now feasible, the on-the-fly computation of the potential energy in any molecular dynamic calculations can be a computationally

expensive or unaffordable task, and issues such as a balance between the computer resources available and the desired accuracy should be considered. In this sense, the development of efficient and automatic schemes has been for a long time the cornerstone in computational molecular science research. Machine learning (ML) has become a popular and promising approach[43–48] due to its ability to learn patterns in data without being explicitly programmed. Thus, machine learned PESs can identify an unbiased unknown function *via* training with a set of known molecular structures and energies.[49–52] In this way they have become valuable and powerful tools in studying various physical–chemical processes, such as the vibrational analysis of a molecule, reducing both computational cost and efforts, as they can be directly evaluated without repetition of setup steps. Currently, most ML algorithms used for the PESs construction are either kernel-based or neural network (NN)-based representations.[53–58] The NN approaches are computationally efficient for multidimensional PESs, while kernel-based methods are more advantageous for small molecules, and they have become very attractive thanks to their effectiveness in describing high system nonlinear functions, even for small training sets. In particular, the RKHS approach[59–62] reproduces exactly by construction all training data and at the same time captures correctly the asymptotic long-range potential interactions *via* appropriate kernel polynomials.[63–67]

Therefore, the purpose of this research is to generate a full kernel-based machine-learning potential energy surface for the $[Ar_2H]^+$ molecule, trained on high quality CCSD(T)/CBS data, which would be capable of accurate predictions of energetics and spectroscopic properties for its known isotopologues, aiming to facilitate the astrochemical detection of such noble gas compounds in new ISM regions. Here, the strategy to develop a highly accurate kernel-based ML-PES will be discussed in detail and the results obtained will be compared with those from available literature.

1 Computational methods, results and discussion

1.1 Building up kernel-based ML-PESs

Of all the different ML-approaches, we chose here the kernel-methods, which are one of the most popular options due to their successful results with small training sets. These are defined as learning algorithms based on the memory of the training data set to predict a new value as a result of a linear combination of similarity basis functions, the well-known kernel functions. There are multiple kernel functions (such as the polynomial kernel, Gaussian kernel or hyperbolic tangent kernel) whose predictive performances depend on the representation of the data. Consequently, the main goal of these ML-schemes is to accurately select the kernel function that best suits the data set.

In this work, we will focus on the RKHS method proposed by Ho and Rabitz,[59] which has proven to be an excellent option to generate accurate predictions of spectroscopy properties as well

This journal is © the Owner Societies 2024

Phys. Chem. Chem. Phys., 2024, **26**, 7060–7071 | **7061**

as in molecular dynamics applications. Furthermore, for small molecular system (species that do not exceed three atoms in their structure, such as in the case in this study) is able to reproduce smoothly all data training set in all different regions of the potential with RMSE values almost non-existent. Briefly, the full-PES form is written in matrix-form,

$$
\begin{bmatrix} V_1 \\ V_2 \\ \vdots \\ V_N \end{bmatrix} = \begin{bmatrix} \alpha_1 \\ \alpha_2 \\ \vdots \\ \alpha_N \end{bmatrix} \begin{bmatrix} K(x_1, x_1') & K(x_1, x_2') & \cdots & K(x_1, x_N') \\ K(x_2, x_1') & K(x_2, x_2') & \cdots & K(x_2, x_N') \\ \vdots & \vdots & \ddots & \vdots \\ K(x_N, x_1') & K(x_N, x_2') & \cdots & K(x_N, x_N') \end{bmatrix}
$$

(1)

where α_i are the coefficients, $K(x, x_i')$ is the reproducing kernel function and x_i' represents the training data set, which are the geometries for which energies, V_i, have been determined from electronic structure calculations. The multidimensional kernel can be written as a direct product $K(x, x_i') = \prod_{j=1}^{M} k_j(x, x_i')$, with M being the dimension of the problem, and $k_j(x, x_i')$ being the one-dimensional reproducing kernels for each one. The triatomic system under study is described by Jacobi coordinates (r, R, θ), where r is the ArH$^+$ bond length, R is the intermolecular distance of the Ar atom from the center of mass of the diatom, and θ is the angle between the r and R vectors. In this way, eqn (1) takes the following form:

$$
V(r, R, \theta) = \sum_{i=1}^{N_r} \sum_{j=1}^{N_R} \sum_{k=1}^{N_\theta} \alpha_{ijk} q_1^{n',m'}(r_i, r) q_2^{n,m}(R_j, R) q_3(z_k, z) \quad (2)
$$

with $q_1^{n',m'}$, $q_2^{n,m}$ and q_3 being the one-dimensional kernel functions for the diatom distance-like (r), the Ar-diatom distance-like (R), and angle-like (θ) variables, respectively. In the above

equation, the reduced coordinate is $z = \cos\theta$, whereas, N_r, N_R and N_θ are the number of *ab initio* calculated points in each coordinate. The reproducing distance-like kernel functions q_1 and q_2 are represented by the same form,

$$
q_{1,2}^{n,m} = n^2 \chi_>^{-(m+1)} B(m+1, n)_2
$$

$$
\times F_1\left(-n+1, m+1; n+m+1; \frac{\chi_<}{\chi_>}\right)
$$

(3)

where $\chi = r$ or R, respectively, $\chi_>$ and $\chi_<$ are the larger and smaller of the χ, respectively, and the angle-like kernel function is given as $q_3(z, z') = \sum_{ll} \frac{(2ll+1)}{2} P_{ll}(z) P_{ll}(z')$. The n and m superscripts refer to the order of smoothness of the function and its asymptotic behavior at large distances, with $n = 2$, and $m = 3$ accounting for the R^{-4} leading dispersion interaction between the Ar atom and ArH$^+$ molecular ion. B is the beta function, $_2F_1$ is the Gauss hyper-geometric function, and P_{ll} is the Legendre polynomials with $ll = 0$–18.

In turn, in Fig. 1 a general flowchart is displayed summarizing the main steps in constructing kernel-based ML PESs:

• Data generation: this first step is the most crucial in the construction of an accurate PES, as the sampling of the data should be representative of the entire configuration space, especially those in physically important regions, and benchmarking the performance of *ab initio* methods, as well as computational resources should be adequately evaluated.

• Data preprocessing: this step consists of organizing the data and removing possible errors or inconsistencies, which may be present, allowing the extraction of meaningful information.
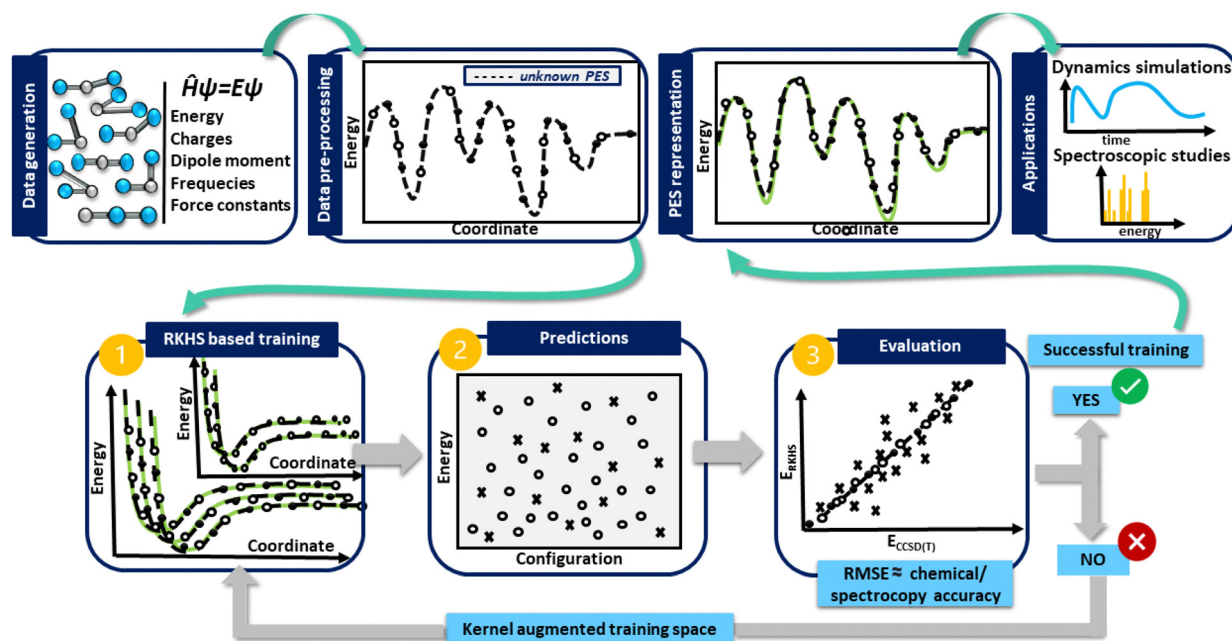

Fig. 1 Schematic representation of the kernel-based ML-PES protocol.

● Data preparation: at this stage the generated data are split into two subsets for training and testing. During the training, the kernel functions interpolate the training reference/*ab initio* set of data, reproducing them with excellent accuracy, while in the testing, the prediction of the trained model is estimated, and its under- or over-estimation error is evaluated. If the error obtained is greater than the established limited, then the kernel space training must be increased until successful results are obtained.

● PES model evaluation and production: at this point, the test set becomes important, as its data allow the performance of the model to be estimated. As a measure of its overall accuracy, it is common to compute the root-mean-square errors (RMSE) of the test data set. Once the evaluation/testing stage is completed, the ML-PES is able to make accurate predictions and then, it is ready to be used for some production task in a variety of molecular dynamics and/or spectroscopic studies.

Next, we address in detail each of these steps followed in the present PES construction.

1.2 Data generation and preprocessing: assessing electronic structure calculations

All *ab initio* electronic structure calculations were performed with the MOLPRO 2022 program,[68] while the DENEB software package[69] was employed to generate and organize all input and output data files, respectively.

1.2.1 [Ar$_2$H]$^+$ optimized structures. We started by performing optimization calculations at the CCSD(T)/aug-cc-pV6Z level of theory, followed by the corresponding harmonic normal mode frequency analysis. As in previous studies[22,25,26,29] we found that the optimized equilibrium structure of the triatomic [Ar$_2$H]$^+$ complex shows a linear Ar–H$^+$–Ar configuration, belonging to the $D_{\infty h}$ point of the group, with Ar–H$^+$ bond lengths of 1.5056 Å and a total energy of -1054.34945185 a.u. (see Fig. 2). We should highlight that the Ar–H$^+$ bond lengths in the Ar$_2$H$^+$ are larger compared with that of 1.2810 Å in the isolated [ArH]$^+$ molecule,[8] as the incorporation of the new Ar atom causes distortion in the electronic density generating the elongation of the bond. As shown in Fig. 2, another linear optimized structure corresponding to Ar–Ar–H$^+$ geometry (local minimum) is found at an energy of 4767 cm^{-1} above the global minimum, with Ar–Ar and Ar–H$^+$ bond lengths of 3.1233 and 1.2801 Å, respectively, while the transition state structure between the two equilibrium configurations, 4478 cm^{-1} higher than the global minimum, has a bent geometry with $\angle \theta = 109.5°$ and Ar–Ar and Ar–H$^+$ bond lengths of 3.3967 and 1.2810 Å, respectively.

The harmonic vibrational frequencies for the ^{40}Ar–H$^+$–^{40}Ar structure from the CCSD(T)/AV6Z computations are shown in Fig. 2, with the cation possessing four vibrational degrees of freedom: the symmetric Ar–H$^+$ stretching (ν_1) at 322.82 cm^{-1}, which is also known as the intermolecular Ar···Ar stretch, the degenerate proton (H$^+$) bending (ν_2) at 680.34 cm^{-1}, and the asymmetric Ar–H$^+$ stretching (ν_3) at 959.08 cm^{-1}, which is also known as the shared-proton stretching. The calculated harmonic zero-point-energy (ZPE) value is 1321.29 cm^{-1}, with the harmonic vibrational frequencies being in line with the values
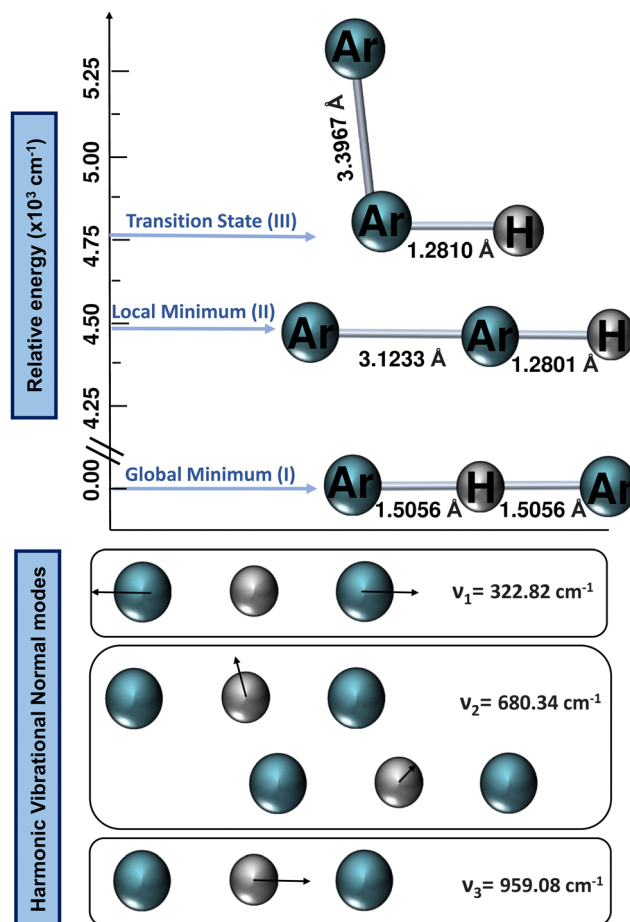

Fig. 2 Optimized equilibrium and transition state structures of [Ar$_2$H]$^+$ from CCSD(T)/AV6Z computations (upper panel). Visualization of the calculated harmonic vibrational normal modes of the global minimum ^{40}Ar–H$^+$–^{40}Ar conformer.

reported in previous QCISD/6-311++G(3df,3pd), MP2/AVQZ, CCSD(T)/AVQZ, and CCSD(T)/AV5Z studies,[22,25,26,29] as well as their corresponding intensities, with that of the shared-proton stretching mode presenting a high value of 4894 km mol^{-1} compared to the ν_2 mode of 46.3 km mol^{-1}, indicating the presence of this ν_3 bright mode in the IR spectra.

1.2.2 [Ar$_2$H]$^+$ dissociative pathways. Next, we examined the energetics of possible dissociation channels, and according to the CCSD(T)/AV6Z calculation (see Fig. 3), the most likely direct dissociation pathway for the [ArHAr]$^+$ complex is into a Ar atom and ArH$^+$ molecular cation, situated at a relative energy of 5317 cm^{-1}. As all fundamental vibrational frequencies are below this value, vibrational transitions can be detected, as well as a pure rotational spectrum if the conditions are adequate for its formation in the ISM. The next-lowest dissociation mechanism is for [Ar$_2$H]$^+$ to lose a hydrogen cation to form Ar$_2$, with its energy cost being nearly seven times more than its predecessor at 35 951 cm^{-1}, while the CCSD(T)/AV6Z dissociation energies for the following channels are 38 012, 45 073, 55 900, and 55 940 cm^{-1}, respectively. Therefore, given that the most likely way for [Ar$_2$H]$^+$ to dissociate, and to do so by a wide

This journal is © the Owner Societies 2024
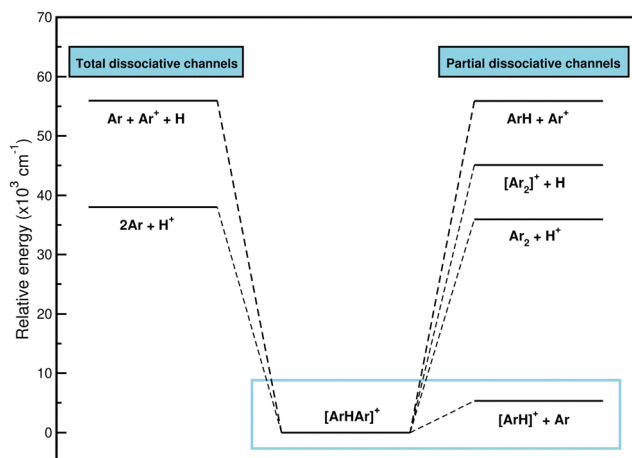
Phys. Chem. Chem. Phys., 2024, **26**, 7060–7071 | **7063**

Fig. 3 Energetics of the dissociation pathways of Ar_2H^+ from the CCSD(T)/AV6Z computations.

margin, is to form ArH^+ and an Ar atom, it seems likely that $[Ar_2H]^+$ is a precursor to the formation of ArH^+. For that reason, the study of the interaction will focus on the dissociation of the system to the lowest $[ArH]^+ + Ar$ channel.

In Table 1 we list the stepwise formation energies as the Ar atoms are bound around the proton, and one can compare the presented results to those previously reported.[22,25,26,29] The binding of the first Ar to H^+ produces a strong bound dimer, while the interaction is much weaker when the second Ar is bound to the ArH^+, as evident from the calculated first- and second-step formation energies in Table 1. The overall formation energy at $T = 0$ K for the $[Ar_2H]^+$ is calculated by summing the stepwise formation energies, with the contribution of the first-step dictating the overall behavior. By comparing with previously reported data, the differences found are clearly due to the different methods and basis sets employed, such as the data of ref. 22 and 26, respectively. In the case of the reported values in ref. 25 and 29 the energy differences of ≈ 2 kcal mol^{-1} come from the fact that the CCSD(T) and CCSD(T)/AV5Z calculations have been carried out without including the basis set superposition error (BSSE) correction. One can see that even when large basis sets were used the BSSE is still important, as it could lead to an overestimation of the binding in molecular systems.

1.2.3 Reference data from electronic structure calculations. As mentioned, the quality of the data sets depends on the accuracy of the electronic structure calculations, involving both the level of theory and basis set employed, while the amount of data is limited by the efficiency of the implemented method/code and computational resources available. For that reason, different levels of theory such as the second order Møller–Plesset perturbation (MP2),[70] single and double excitation coupled cluster with perturbative triples (CCSD(T)),[71] as well as explicit correlated F12 methods,[72] as implemented in the MOLPRO package,[68] were employed to compute the total and interaction energies of the complex at various geometries. In total 35 340 energies were computed at a grid of the intermolecular r and R distances ranging from 0.8 to 2.3 Å and 1.8 to 8.0 Å, respectively, and for θ angles between 0–180°, using the correlation-consistent basis sets,[73–75] such as AVQZ, AV5Z and AV6Z. The criterion for the selection of the AVnZ, n = Q-6, basis sets in this study is based on the analysis reported in our previous work.[8] The impact of the BSSE is also evaluated, through the counterpoise correction (CP),[76] as $E_{BSSE}([Ar_2H]^+) = \left(E_{[ArH]^+}^{[Ar_2H]^+}([Ar_2H]^+) - E_{[ArH]^+}^{[ArH]^+}([ArH]^+) \right) + \left(E_{Ar}^{[Ar_2H]^+}(Ar) - E_{Ar}^{Ar}(Ar) \right)$, where $E_{[ArH]^+}^{[Ar_2H]^+}([Ar_2H]^+)$ and $E_{Ar}^{[Ar_2H]^+}(Ar)$ are the energies of $[ArH]^+$ and Ar using the $[Ar_2H]^+$ basis functions, while $E_{[ArH]^+}^{[ArH]^+}([ArH]^+)$ and $E_{Ar^+}^{Ar}(Ar)$ are the energies of $[ArH]^+$ and Ar, respectively. We also performed extrapolation of the correlation energies utilizing the two-point single inverse power function first introduced by Schwartz[77] $E_n = E_{CBS} + \dfrac{A}{n^3}$, with $n = 5$ and 6, in order to obtain the energy at the complete basis set (CBS) limit.

Fig. S1 (see the ESI†) shows representative plots of the total energy of $[Ar_2H]^+$ as a function of R and θ, while in Fig. S2 (ESI†) one can see the BSSE corrections to the energy as a function of the *ab initio* method, MP2, CSSD(T) and CCSD(T)-F12, and the cardinal number n of the AVnZ basis sets. In both figures the estimates of the corresponding CBS[56] extrapolation are also displayed. As expected, the CCSD(T) total energies are lower than those obtained from the MP2 calculations, the increment of the basis set produces a further lowering in the total energy and a decrease in BSSE, being the extrapolation to the CBS limit the one that reduces it almost to zero. The case of the CCSD(T)-F12 calculations should be highlighted, where the BSSE error is significantly reduced. On the basis of such evaluation tests, the CCSD(T)/CBS[56] level of theory has been chosen for the

Table 1 Formation energies in kcal mol^{-1} for ArH^+–Ar at its linear configuration using the indicated basis sets and level of theory.[22,25,26,29] A comparison with theoretical values from previous studies is also presented

	First-step $Ar_{(g)} + H_{(g)}^+ \rightarrow [ArH]_{(g)}^+$	Second-step $[ArH]_{(g)}^+ + Ar_{(g)} \rightarrow [Ar_2H]_{(g)}^+$	Overall formation $2Ar_{(g)} + H_{(g)}^+ \rightarrow [Ar_2H]_{(g)}^+$
QCISD/6-311++G(3df,3pd)[22]	−96.01	−14.30	−110.13
MP2/AVQZ[26]	−91.86	−15.66	−107.52
CCSD(T)/AVQZ[29]	−93.96	−15.56	−109.52
CCSD(T)/AV5Z[25]	−94.10	−16.60	−110.70
CCSD(T)/AV5Z	−92.94	−15.46	−108.40
CCSD(T)/AV6Z	−93.28	−15.31	−108.59
CCSD(T)/CBS[56]	−93.57	−15.14	−108.71

7064 | *Phys. Chem. Chem. Phys.*, 2024, **26**, 7060–7071

This journal is © the Owner Societies 2024

generation of the reference data sets in this study, with the reference structures sampled in a 3D (r,R,θ) grid.

1.3 Representation of the RKHS ML-PES model: training, validation and testing

In order to assess the quality of the results obtained with the ML-potential, an action protocol was introduced to validate the RKHS-based ML-PES. This consists of three clearly differentiated stages.

1. Analysis of the resulting learning model potential at the same sets of points involved in the training procedure was carried out to ensure the reproducibility of the results obtained.

2. Production of new potential values outside the range of the input points (validation/testing data sets).

3. Monitoring regression diagnostics, such as a root mean square error (RMSE) threshold criterion with respect to the testing datasets should be fulfilled, otherwise more training data should be added.

1.3.1 Data preparation: grids and energy distributions. In this way, application of the kernel-based protocol implied an attempt to increase the size of datasets up to 13 680 CCSD(T)/CBS[56] *ab initio* points in the training procedure. The latter are equally distributed in a 16-points grid in the r coordinate ranging between 0.8 and 2.3 Å, a 45-points grid in the internuclear distance R from 1.8 to 8.0 Å, and a 19-points grid in the angle θ coordinate between 0 and 180°. We employed twelve sets of training data with 1200/1254, 2280, 2700/2736, 3200/3344, 5130, 6080, 7200/7296 and 13 680 points by choosing with different step sizes corresponding to 6 or 16, 11, 20, 24 or 45, and 10 or 19 in the r, R and θ coordinates, respectively, with all of them covering the same coordinate and energy ranges. In this manner, Fig. 4 depicts histograms of these data sets, showing similar distributions of energies.

Likewise, 21 660 additional configurations and CBS[56] energy data were also generated (see their energy distribution in the right panel of Fig. 5), for the potential evaluation in the
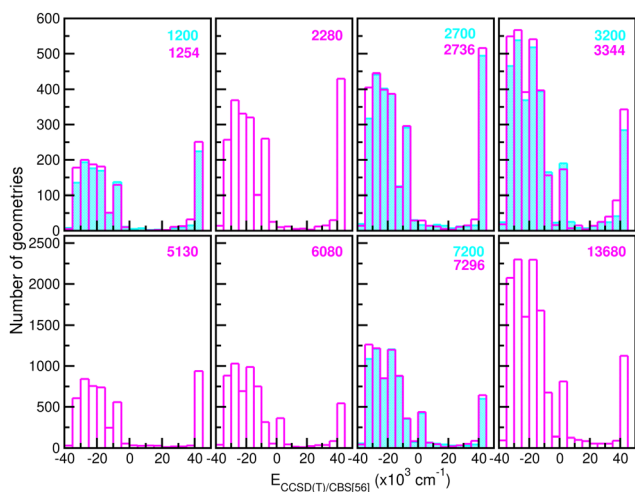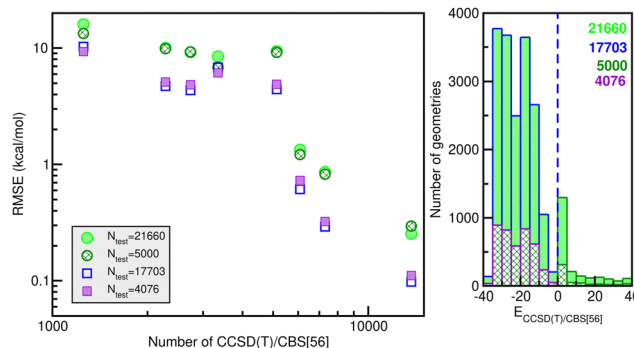

Fig. 5 RMSE values of the RKHS ML-PES models *vs.* the number of training set size (left panel). Histograms of total 21 660 or 17 703 datasets with energies below the dissociation threshold and 5000/4076 randomly chosen testing data sets (right panel), with the blue dashed line indicating the dissociation threshold.

testing stage in order to ensure its quality, as we will discuss next.

1.3.2 Comparative quality analysis: error diagnostics. Fig. 5 shows the systematic improvement of the RMSE of the RKHS ML-PES model with an increasing number of training data. We used a hold-out cross-validation scheme to select the best performing RKHS PES among the twelve trained models. The RMSE values were computed considering the total number of testing data, as well as by averaging the RMSE of 5000 randomly chosen points from the total of 21 660 testing sets. Thus, one can see the quality of the RKHS PES as a function of the size of the training data with 1200/1254, 2280, 2700/2736, 3200/3344, 5130, 6080, 7200/7296 and 13 680 points, shown in Fig. 4. As the size of the dataset increases, the RMSE values are decreasing. We also observed a large sensitivity on the RMSE values with respect to the sampling in the θ coordinate. In particular, we found that the RKHS PES models trained on the 1200 ($6 \times 20 \times 10$), 2700 ($6 \times 45 \times 10$), 3200 ($16 \times 20 \times 10$) and 7200 ($16 \times 45 \times 10$) datasets show much higher RMSE values (ranging between 60–130 kcal mol^{-1}) compared to those obtained from the 1254 ($6 \times 11 \times 19$), 2736 ($6 \times 24 \times 19$), 3344 ($16 \times 11 \times 19$) and 7296 ($16 \times 24 \times 19$) ones (in the 0.1–10 kcal mol^{-1} range). The calculated RMSE values for all RKHS ML-PES models with respect to the total 21 660 test data, 17 703 datasets with energies below the dissociation threshold, and the two corresponding 5000/4076-randomly chosen testing sets show the same behaviour.

The correlation plots shown in Fig. 6 demonstrate the performance of the chosen RKHS ML-PES model compared to the 13 680 training and 21 660 testing data, in both attractive and repulsive regions of the potential. The RMSE values are also displayed as a function of energy ranges (see the right panel of Fig. 6). One can see that the RMSE values outside the training zone are 0.098 kcal mol^{-1} up to dissociation energies over 17 703 configurations (see also the left panel of Fig. 5), and a total mean absolute error (MAE) lower than 0.001% over 21 660 configurations and up to energies of 100 kcal mol^{-1} above dissociation.

Fig. 4 Histograms of different size (see the number given in the top right of each panel) training data sets employed in building up the RKHS ML-PES models.

This journal is © the Owner Societies 2024

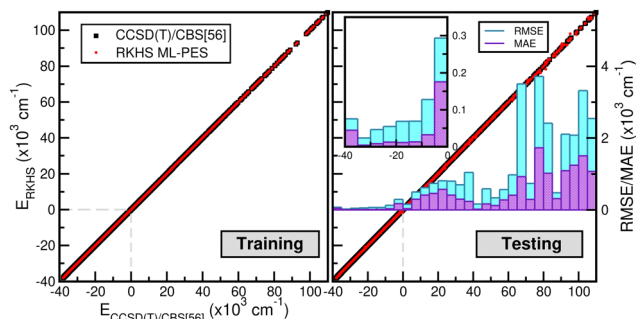*Phys. Chem. Chem. Phys.*, 2024, **26**, 7060–7071 | **7065**

Fig. 6 Correlation plots showing the performance of the RKHS ML-PES against the reference CCSD(T)/CBS[56] energies for both training (left panel) and testing (right panel) data. The RMSE and MAE values are also displayed as a function of CCSD(T)/CBS[56] energies (right panel).
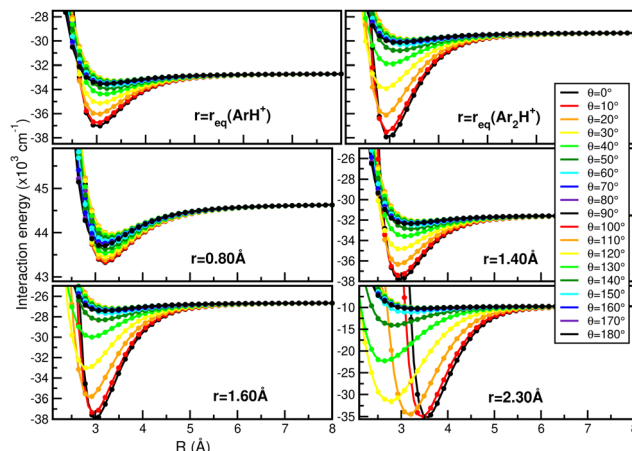

Fig. 7 Comparison of the RKHS ML-PES energies (solid lines) with the CCSD(T)/CBS[56] reference values (circle symbols) as a function of R distance at the indicated θ and r values.

By analysing the overall quality of the RKHS ML-PES, it is observed that the number of training data required for the construction of the ML-PES is lower than or close to those used in other previous studies, such as in ref. 22 and 29. In the first PES,[22] 7400 *ab initio* energies were required in the fitting procedure with an RMSE of 0.143 kcal mol^{-1}, while for the parameterization of the other PES,[29] in total 13 940 *ab initio* energies have been used, and a RMSE of 0.057 kcal mol^{-1} has been reported. These differences are logical, since a greater number of points allows us to obtain *a priori* a better approximation of the values. Nevertheless, it is observed that despite the fact that almost the same number of points has been used for the design of the PES of ref. 22 and ours here, the RMSE of 0.00012 kcal mol^{-1} found in the present RKHS ML-PES is significantly lower for the training set data. This is undoubtedly due to the use of a learning process based on kernel methods that significantly reduces the number of data needed to develop a high-accuracy PES, instead of an analytical potential, as demonstrated in other recently published works.

1.3.3 Orientational anisotropy effects: potential topology. Apart from the typical quantitative error analysis of the RKHS ML-PES, presented in the previous subsection, we also proceed with potential curves plots along representative coordinates of the hydride cation under study.

In this way, Fig. 7 displays comparisons of the present RKHS scheme in different regions of the $[Ar_2H^+]$ potential as a function of the R coordinate for given θ angle values and selected r distances. The upper panels show the RKHS ML potential curves at $r = 1.2801$ and 1.5056 Å, corresponding to the equilibrium bond length of the ArH$^+$ and [ArH$^+$Ar] cations. These configurations form part of the testing data set, while the RKHS potential curves shown in the middle and lower panels of Fig. 7 correspond to configuration and energies with r values in the training range of the CCSD(T)/CBS[56] *ab initio* data. In this way, one can see that the RKHS ML-PES describes smoothly the *ab initio* data for all angular orientations of the system for all cases analyzed.

In turn, particular characteristics of the full 3D RKHS ML-potential for the $[Ar_2H^+]$ cation were also analyzed. Thus, in order to further check the smoothness of the PES, we present

two-dimensional contour plots, as an excellent tool to visualize three-dimensional data in an easy and intuitive way. Therefore, Fig. 8 shows few representative contour plots of the RKHS ML-potential in the (r, R)-plane for linear configurations, and (θ, R)-plane, with r fixed at the equilibrium distances of the ArH$^+$ and ArH$^+$Ar systems.

One can see that the global minimum corresponds to the linear $[Ar-H-Ar]^+$ configuration with a well-depth equal to 38011.37 cm^{-1} (108.68 kcal mol^{-1}) for the ML-PES, located at $R = 2.974$ Å and $r = 1.5058$ Å. The difference between *ab initio* calculations and our algorithm are 0.03 cm^{-1}, almost negligible, indicating that the kernel-based model describes smoothly this region of the $[Ar_2H]^+$ PES. The second PES's minimum coincides with the antilinear configuration of the complex, $[Ar-Ar-H]^+$, with $R = 3.20$ Å and an energy of $-30\,022.97$ cm^{-1} (-85.84 kcal mol^{-1}). Like its predecessor, there is an excellent correlation between the values obtained with the ML-potential and the *ab initio* data for such asymmetric linear configurations. The potential barrier between the global and local potential minima corresponds to the T-shaped configuration at $R = 3.40$ Å with an energy of $-29\,753.66$ cm^{-1} (-85.07 kcal mol^{-1}). Such double-minimum topological aspects of the Ar$_2$H$^+$ ML PES are shown in Fig. 8.

1.4 Bound state calculations: quantum effects on vibrations

In turn, once the quality of the RKHS ML potential is evaluated, we then employed it, by direct potential function implementation at any molecular configuration, to compute vibrational bound states, aiming to investigate the effect of the potential shape on the vibrations and facilitate spectroscopic data for different isotopic species. Bound state calculations were carried out using the DVR3D program[78] by solving the nuclear time-independent Schrödinger equation with an exact kinetic energy operator. We used the Jacobi (r, R, θ) coordinates to represent the Hamiltonian matrix in a 3D discrete variable representation (DVR) grid of points. A Morse-like oscillator basis set was used for the radial r and R coordinates and Gauss-associated
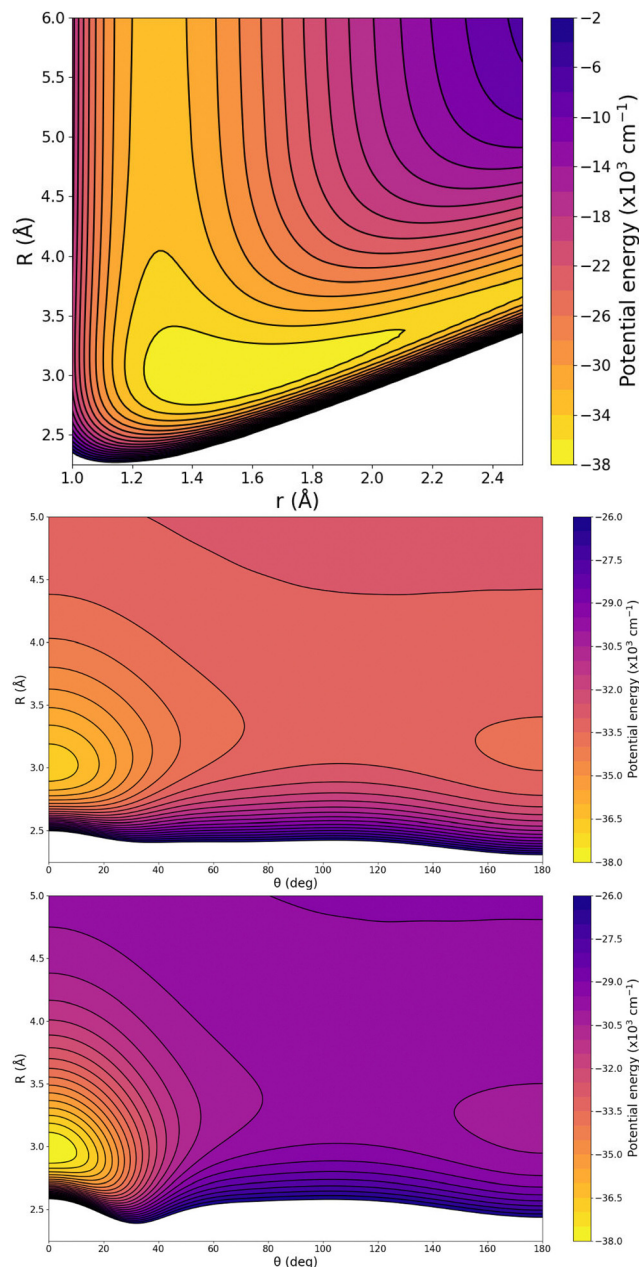
7066 | *Phys. Chem. Chem. Phys.*, 2024, **26**, 7060–7071

This journal is © the Owner Societies 2024

Fig. 8 Two-dimensional contour plots of the RKHS ML-PES for $[Ar_2H]^+$ complex in the (r,R)-plane for $\theta = 0°$ (upper panel) and (θ,R)-plane for $r = 1.2810$ (middle panel) and 1.5056 Å (lower panel). The equipotential curves start at the energy of 38 000 cm^{-1} with intervals of 2000 (upper panel) and 500 cm^{-1} (middle and lower panels).

Legendre functions for the angular coordinate, θ. The parameters of the radial basis set were optimized to ensure convergence of the lowest twenty $J = 0$ energy levels, and as a result the optimal set of D_e, r_e and ω_e Morse parameters were 0.021/0.0016 a.u., 3.45/6.06 a.u. and 0.012/0.00075 a.u. for the r/R grid. Given the importance of different isotopes, due to their abundance in ISM, and thus their potential detection in a variety of astrophysical environments, we decided to consider the ^{36}Ar and ^{40}Ar isotopologues for the spectroscopy analysis. With that purpose and taking into account that the electronic

structure of the different isotopes of the $[Ar_2H]^+$ system is the same, only modifications in the kinetic energy operator involving the mass of Ar and reduced mass of the ArH$^+$ diatom, $\frac{1}{\mu} = \frac{1}{m_{Ar}} + \frac{1}{m_H}$, where $m_{Ar} = 35.967545105/39.9623831225$ and $m_H = 1.00782503207$ a.u. are the nuclear/atomic masses of $^{36/40}Ar$, and H isotopes,[79] respectively, were used. For the evaluation of integrals, 55/55-point Gauss-Laguerre and 60-point Gauss-Legendre quadratures between 0 and 180° were used, for radial and angular coordinates, respectively, with the range of quadrature points in r and R coordinates being 2.07–4.49 a.u., and 4.72–7.07 a.u, respectively.

In this way, the $J = 0$ energy levels calculated with the present Ar$_2$H$^+$ ML-PES are listed in Table S1 (see the ESI†) for the $^{36}Ar/^{40}Ar$ isotopes. One can see that the quantum effects on the vibrational bound states for the two isotopologues of Ar are subtle. The anharmonic ground state energies are found at 1367.0 and 1356.6 cm^{-1} above the global minimum of the PES corresponding to the anharmonic ZPEs of the $^{36}Ar_2H^+$ and $^{40}Ar_2H^+$, respectively. By comparing with the computed harmonic ZPE of 1321.3 cm^{-1} for the $^{40}Ar_2H^+$, one can see that there is a positive anharmonicity counting of 35.3 cm^{-1}, that we will discuss later on each vibrational mode. The anharmonic ZPE of 1376.2 cm^{-1} has been previously reported on a CCSD(T)/AVQZ parameterized PES[29] for $^{40}Ar_2H^+$, which is within 19.6 cm^{-1} of the present value. Moreover, the ZPE values of 1400 and 1391.3 cm^{-1} for $^{36}Ar_2H$ and $^{40}Ar_2H$, respectively, were obtained from a combined CCSD(T)/AV5Z and quartic force field analysis,[25] which are in accord with the present ones within 34.7 cm^{-1} in the $^{40}Ar_2H^+$ case.

In Fig. 9 the calculated bound vibrational energies are plotted together with the minimum energy path of the CCSD(T)/CBS[56] RKHS ML-PES along the θ coordinate by optimizing both r and R radial coordinates, while Fig. 10 displays radial and angular probability distribution plots for a few selected states. By analyzing the nodal structure of the probability density functions for each calculated state, one can
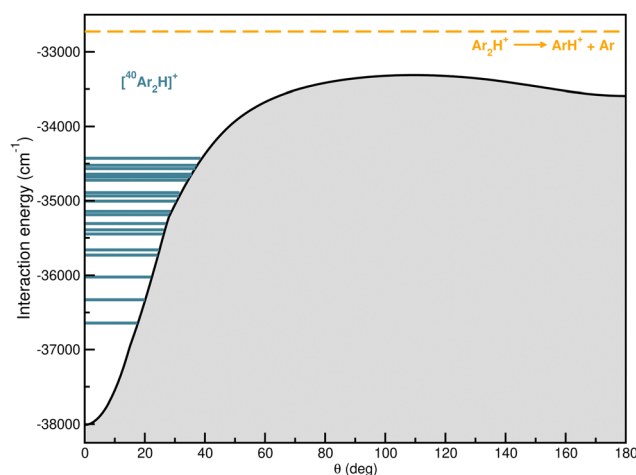

Fig. 9 Minimum energy path for RKHS ML-PES together with the 20 lowest $J = 0$ vibrational states for the $[^{40}Ar_2H]^+$ isotope.

This journal is © the Owner Societies 2024
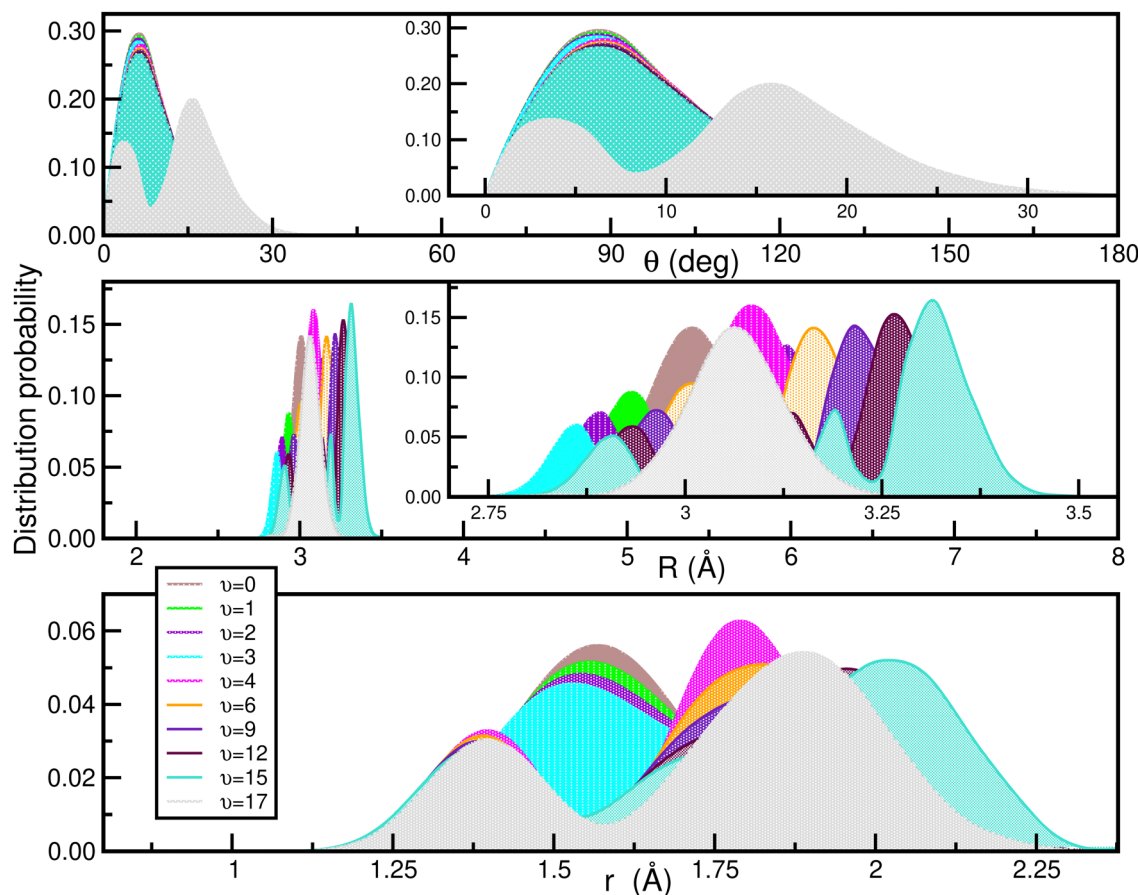
Phys. Chem. Chem. Phys., 2024, **26**, 7060–7071 | **7067**

Fig. 10 Angular (upper panel) and radial (middle and lower) density distributions of the indicated vibrational states of the $[^{40}Ar_2H]^+$ isotope.

Table 2 Comparison of vibrational bands (in cm^{-1}) for the $^{40}Ar_2H^+$ molecule calculated with the present CCSD(T)/CBS[56] RKHS ML-PES to those reported in previous theoretical studies,[25,26,28,29] and experimental, gas-phase[16]/matrix[10,14,15] measurements. In the first two columns the vibrational level number (ν) and a vibrational mode assignment (ν_1, ν_2, ν_3) are given

ν	ν_1, ν_2, ν_3	This work	Theory[abcd]	Expt.[ef]
1	1,0,0	290.7	291.8/292/—/271.4	—/—
2	2,0,0	580.7	579.6/—/—/—	—/—
—	$0,1^1,0$	651.2	660.5/670/—/648	—/—
3	3,0,0	866.2	862.5/—/—/—	—/—
4	0,0,1	977.0	994.3/986/1000/1094.7	989/905,903,903.8
6	1,0,1	1238.7	1246.8/1237/1253/—	1237/—
9	2,0,1	1492.2	1493.3/1484/1500/—	1485/—
12	3,0,1	1732.1	1732.8/1730/1750/—	1726/—
15	4,0,1	1958.8	1964.8/1989/—/—	2041/—
17	0,1,1	2094.6	2133.3/2136/—/—	2124/—

[a] Ref. 29. [b] Ref. 28. [c] Ref. 26. [d] Ref. 25. [e] Ref. 16. [f] Ref. 10, 14 and 15.

extract the corresponding assignment, and thus states have been assigned according to the ν_1, ν_2 and ν_3 vibrational quantum numbers.

Likewise, the vibrational bands (in cm^{-1}) for the $[^{40}ArH]^+$ are collected in Table 2, and their values are compared with recent theoretical calculations,[25,26,28,29] as well as experimental data

from gas phase infrared photodissociation spectra (IRPD),[16] and matrix infrared spectral measurements in Ar/H_2 mixtures[10] and doped noble-gas matrices[14,15] available in the literature. One can actually see that experimental measurements are available for the fundamental asymmetric stretching, ν_3, frequency in gas-phase and matrix environments,[10,14–16] with the gas-phase value of 989 cm^{-1} being higher than those of 905, 903.8 and 903 cm^{-1} in the Ar-matrix. Our prediction at 977.0 cm^{-1} is within 12 cm^{-1} from the gas-phase experimental value for the Ar_2H^+. Next, the fundamental symmetric stretching, ν_1, frequency for Ar_2H^+ is calculated at 290.7 cm^{-1} in close accord to previously computational reported estimates,[25,28,29] while the fundamental ν_2 bending frequency, obtained from $J = 1$ DVR3D calculations, is 651.2 cm^{-1}, within 3–20 cm^{-1} from the previously calculated values of 660.5, 670 and 648 cm^{-1} given in ref. 25, 28, and 29 (see Table 2).

Also, we should point out that by comparing with the normal harmonic mode frequencies we found that they differ by 20 and 30 cm^{-1} approximately (see Fig. 2), suggesting that the anharmonic effects in this complex are considerable. In addition, comparisons of the predicted $n\nu_1 + \nu_3$ combination bands (with $n = 1–4$) with those experimental measurements reported[16] from IR photodissociation spectroscopy for the $[Ar_3H]^+$ are also shown in Table 2. We can observe that they are in reasonable

7068 | *Phys. Chem. Chem. Phys.*, 2024, **26**, 7060–7071

This journal is © the Owner Societies 2024

accord, within an error less than 7 cm^{-1}, except for the $4\nu_1 + \nu_3$ with a difference of around 80 cm^{-1} (see Table 2). All these results seem to indicate that the ML-PES constructed in this work makes a realistic prediction for the $[Ar_2H]^+$ complex. Moreover, as previously suggested,[16,23,80] this finding could also indicate that this system is the core for more large argon hydrides, $[Ar_nH]^+$, and cations.

2 Summary and conclusions

This work was motivated by the previous knowledge that theoretical quantum chemistry treatments could provide useful spectroscopic data for the detection of new molecules in the laboratory experiments or even in the ISM. Nowadays, the use of quantum chemistry calculations in astrochemical detection has become standard for species that have not even been synthesized in the laboratory, and high-quality data is in demand. Naturally-occurring noble gas molecules are part of such compounds, and will be likely dominated by Ar. Furthermore, advances within the field of machine learning provide higher-level, more flexible and adaptive approaches compared to traditional methods for PESs construction, making it a powerful tool within theoretical chemistry.

Thus, the present study focused on the quantum chemical, spectroscopic analysis of the $[Ar_2H]^+$ molecule, that was previously shown to present at least a stable minimum on its potential surface, although for such species spectroscopic data are scarce/limited or still have no available date especially those determined from fully coupled computations. The $[Ar_2H]^+$, in terms of structure, is the simplest form of a protonated cluster, and at first glance, this triatomic system is small enough for constructing a full-dimensional potential surface. Due to its high symmetry, conventional theoretical techniques could be used for its fundamental vibrational analysis, although for higher vibrational transitions significant vibrational coupling is present requiring fully coupled treatments. Therefore, here we evaluated the performance of different high-level *ab initio* electronic structure methods, and interactions energies from CCSD(T)/CSB[56] calculations at a broad grid of intermolecular R distances and the whole range of angular configurations are obtained. These energies were divided into training and testing data for the construction of a 3D ML-PES based on a RKHS scheme. To ensure the robustness of the ML-algorithm used, a potential validation protocol was developed, obtaining a low RMSE value with respect the *ab initio* energies. The RKHS ML PES was found to describe the main aspects of the underlying interactions, and was then used to perform bound state calculations for determining quantum anharmonic effects. Vibrational states were computed and vibrational bands were appropriately assigned to specific quantum excitations. The corresponding transition frequencies for both fundamentals and few overtone progressions were found to compare well with the available experimental data in the literature.

Consequently, this work treats accuracy issues in developing potential interaction ML models that can then provide useful data for the spectral characterization of such proton-bound Ng-containing complexes, and will enhance and/or assist further laboratory, modelling and interstellar studies for detecting such natural Ng molecules in the ISM.

Data availability

The data that support the findings of this study are available within the article and its ESI,† as well as from the authors upon reasonable request.

Author contributions

The authors confirm contributions to the paper as follows: M. J. MOE (data curation, formal analysis, investigation, methodology, validation, writing – original draft preparation), A. V. (data curation, formal analysis, investigation, writing – review and editing), R. P. (funding acquisition, project administration, conceptualization, formal analysis, investigation, methodology, validation, writing – review and editing).

Conflicts of interest

There are no conflicts to declare.

Acknowledgements

Notes and references

1 R. Güsten, H. Wiesemeyer, D. Neufeld, K. Menten, U. Graf, K. Jacobs, B. Klein, O. Ricken, C. Risacher and J. Stutzki, *Nature*, 2019, **568**, 357–359.

2 M. Barlow, B. Swinyard, P. Owen, J. Cernicharo, H. Gomez, R. Ivison, O. Krause, T. Lim, M. Matsuura, S. Miller, G. Olofsson and E. Polehampton, *Science*, 2013, **342**, 1343–1345.

3 H. Müller, S. Muller, P. Schilke, E. Bergin, J. Black, M. Gerin, D. Lis, D. Neufeld and S. Suri, *Astron. Astrophys.*, 2015, **582**, L4.

4 F. Pauzat and Y. Ellinger, *Planet. Space Sci.*, 2005, **53**, 1389–1399.

5 F. Pauzat and Y. Ellinger, *J. Chem. Phys.*, 2007, **127**, 014308.

6 F. Pauzat, Y. Ellinger, J. Pilmé and O. Mousis, *J. Chem. Phys.*, 2009, **130**, 174313.

This journal is © the Owner Societies 2024

Phys. Chem. Chem. Phys., 2024, **26**, 7060–7071 | 7069

7 F. Pauzat, Y. Ellinger, O. Mousis, M. Ali-Dib and O. Ozgurel, *Astrophys. J.*, 2013, **777**, 29.

8 M. Montes de Oca-Estévez and R. Prosmiti, *Front. Chem.*, 2021, **9**, 187.

9 M. Montes de Oca-Estévez and R. Prosmiti, *J. Mol. Graphics Modell.*, 2023, **124**, 108562.

10 V. E. Bondybey and G. C. Pimentel, *J. Chem. Phys.*, 1972, **56**, 3832–3836.

11 D. E. Milligan and M. E. Jacox, *J. Mol. Spectrosc.*, 1973, **46**, 460–469.

12 C. A. Wight, B. S. Ault and L. Andrews, *J. Chem. Phys.*, 1976, **65**, 1244–1249.

13 H. Kunttu, J. Seetula, M. Räsänen and V. A. Apkarian, *J. Chem. Phys.*, 1992, **96**, 5630–5635.

14 H. M. Kunttu and J. A. Seetula, *Chem. Phys.*, 1994, **189**, 273–292.

15 T. D. Fridgen and J. M. Parnis, *J. Chem. Phys.*, 1998, **109**, 2155–2161.

16 D. C. McDonald, D. T. Mauney, D. Leicht, J. H. Marks, J. A. Tan, J.-L. Kuo and M. A. Duncan, *J. Chem. Phys.*, 2016, **145**, 231101.

17 G. Hvistendahl, O. W. Saastad and E. Uggerud, *Int. J. Mass Spectrom.*, 1990, **98**, 167–177.

18 J. Lundell and H. Kunttu, *J. Phys. Chem.*, 1992, **96**, 9774–9781.

19 J. Nieminen and E. Kauppi, *Chem. Phys. Lett.*, 1994, **217**, 31–35.

20 J. Lundell, *J. Mol. Struct.*, 1995, **355**, 291–297.

21 T. D. Fridgen and J. M. Parnis, *J. Chem. Phys.*, 1998, **109**, 2162–2168.

22 J. Y. Qu, W. Li, R. Guo and X. S. Zhao, *J. Chem. Phys.*, 2002, **117**, 2592–2598.

23 K. T. Giju, S. Roszak and J. Leszczynski, *J. Chem. Phys.*, 2002, **117**, 4803–4809.

24 S. J. Grabowski, J. M. Ugalde, D. M. Andrada and G. Frenking, *Eur. J. Chem.*, 2016, **22**, 11317–11328.

25 R. C. Fortenberry, *ACS Earth Space Chem.*, 2017, **1**, 60–69.

26 J. A. Tan and J.-L. Kuo, *J. Chem. Phys.*, 2019, **150**, 124305.

27 R. M. García-Vázquez, M. Márquez-Mijares, J. Rubayo-Soneira and O. Denis-Alpizar, *Astron. Astrophys.*, 2019, **631**, A86.

28 J. A. Tan and J.-L. Kuo, *J. Phys. Chem. A*, 2020, **124**, 7726–7734.

29 D. Koner, *J. Chem. Phys.*, 2021, **154**, 054303.

30 F. Grandinetti, *Front. Chem.*, 2020, **8**, 462.

31 S. Borocci, F. Grandinetti and N. Sanna, *Molecules*, 2021, **26**, 1305.

32 M. Montes de Oca-Estévez, B. Darna, B. García-Ruíz, R. Prosmiti, T. González-Lezana and D. Koner, *ChemPhysChem*, 2023, **24**, e202300450.

33 J.-Y. Lee, K. Marti, J. P. Severinghaus, K. Kawamura, H.-S. Yoo, J. B. Lee and J. S. Kim, *Geochim. Cosmochim. Acta*, 2006, **70**, 4507–4512.

34 R. Wieler, *Rev. Mineral. Geochem.*, 2002, **47**, 21–70.

35 O. L. Polyansky, R. Prosmiti, W. Klopper and J. Tennyson, *Mol. Phys.*, 2000, **98**, 261–273.

36 R. Prosmiti, A. Buchachenko, P. Villarreal and G. Delgado-Barrio, *Theor. Chem. Acc.*, 2001, **106**, 426–433.

37 X. Huang, B. J. Braams, J. M. Bowman, R. E. A. Kelly, J. Tennyson, G. C. Groenenboom and A. van der Avoird, *J. Chem. Phys.*, 2008, **128**, 034312.

38 B. J. Braams and J. M. Bowman, *Int. Rev. Phys. Chem.*, 2009, **28**, 577–606.

39 A. Aguado, P. Barragán, R. Prosmiti, G. Delgado-Barrio, P. Villarreal and O. Roncero, *J. Chem. Phys.*, 2010, **133**, 024306.

40 P. Barragán, R. Prosmiti, Y. Wang and J. Bowman, *J. Chem. Phys.*, 2012, **136**, 224302.

41 D. J. Arismendi-Arrieta, M. Riera, P. Bajaj, R. Prosmiti and F. Paesani, *J. Phys. Chem. B*, 2016, **120**, 1822–1832.

42 C. E. M. Goncalves, B. R. L. Galvão, V. C. Mota, J. P. Braga and A. J. C. Varandas, *J. Phys. Chem. A*, 2018, **122**, 4198–4207.

43 O. T. Unke, D. Koner, S. Patra, S. Käser and M. Meuwly, *Mach. Learn. Sci. Technol.*, 2020, **1**, 013001.

44 F. Noé, A. Tkatchenko, K.-R. Müller and C. Clementi, *Annu. Rev. Phys. Chem.*, 2020, **71**, 361–390.

45 P. O. Dral, *J. Phys. Chem. Lett.*, 2020, **11**, 2336–2347.

46 Q. Tong, P. Gao, H. Liu, Y. Xie, J. Lv, Y. Wang and J. Zhao, *J. Phys. Chem. Lett.*, 2020, **11**, 8710–8720.

47 O. T. Unke, S. Chmiela, H. E. Sauceda, M. Gastegger, I. Poltavsky, K. T. Schütt, A. Tkatchenko and K.-R. Müller, *Chem. Rev.*, 2021, **121**, 10142–10186.

48 M. Pinheiro, F. Ge, N. Ferré, P. O. Dral and M. Barbatti, *Chem. Sci.*, 2021, **12**, 14396–14413.

49 J. Behler and M. Parrinello, *Phys. Rev. Lett.*, 2007, **98**, 146401.

50 J. Behler, *J. Chem. Phys.*, 2016, **145**, 170901.

51 S. Manzhos and T. J. Carrington, *Chem. Rev.*, 2021, **121**, 10187–10217.

52 T. Zubatiuk and O. Isayev, *Acc. Chem. Res.*, 2021, **54**, 1575–1585.

53 P. O. Dral, *J. Comput. Chem.*, 2019, **40**, 2339–2347.

54 A. S. Abbott, J. M. Turney, B. Zhang, D. G. A. Smith, D. Altarawy and H. F. I. Schaefer, *J. Chem. Theory Comput.*, 2019, **15**, 4386–4398.

55 O. T. Unke and M. Meuwly, *J. Chem. Theory Comput.*, 2019, **15**, 3678–3693.

56 S. Chmiela, H. E. Sauceda, I. Poltavsky, K.-R. Müller and A. Tkatchenko, *Comput. Phys. Commun.*, 2019, **240**, 38–45.

57 Y. Shao, M. Hellström, P. D. Mitev, L. Knijff and C. Zhang, *J. Chem. Inf. Model.*, 2020, **60**, 1184–1193.

58 X. Gao, F. Ramezanghorbani, O. Isayev, J. S. Smith and A. E. Roitberg, *J. Chem. Inf. Model.*, 2020, **60**, 3408–3415.

59 T. Ho and H. Rabitz, *J. Chem. Phys.*, 1996, **104**, 2584–2597.

60 T. Hollebeek, T.-S. Ho and H. Rabitz, *J. Chem. Phys.*, 1997, **106**, 7223–7227.

61 T. Hollebeek, T.-S. Ho and H. Rabitz, *Annu. Rev. Phys. Chem.*, 1999, **50**, 537–570.

62 T. Ho and H. Rabitz, *J. Chem. Phys.*, 2003, **119**, 6433–6442.

63 T. Ho and H. Rabitz, *J. Chem. Phys.*, 2000, **113**, 3960–3968.

64 L. Delgado-Tellez, A. Valdés, R. Prosmiti, P. Villarreal and G. Delgado-Barrio, *Int. J. Quantum Chem.*, 2012, **112**, 2971–2975.

7070 | *Phys. Chem. Chem. Phys.*, 2024, **26**, 7060–7071

This journal is © the Owner Societies 2024

65 A. Kalemos, A. Valdés and R. Prosmiti, *J. Chem. Phys.*, 2012, **137**, 034303.

66 N. Alharzali, H. Berriche, P. Villarreal and R. Prosmiti, *J. Phys. Chem. A*, 2019, **123**, 7814–7821.

67 N. Alharzali, R. Rodríguez-Segundo and R. Prosmiti, *Phys. Chem. Chem. Phys.*, 2021, **23**, 7849–7859.

68 H.-J. Werner, P. Knowles, G. Knizia, F. Manby and M. Schütz, *et al.*, *MOLPRO, version 2022.2, a package of ab initio programs*, 2022, see **https://www.molpro.net**.

69 *DENEB 1.30 beta: The Nanotechnology Software by Atelgraphics*, 2020.

70 C. Møller and M. S. Plesset, *Phys. Rev.*, 1934, **46**, 618–622.

71 K. Raghavachari, G. W. Trucks, J. A. Pople and M. Head-Gordon, *Chem. Phys. Lett.*, 1989, **157**, 479–483.

72 W. Györffy and H.-J. Werner, *J. Chem. Phys.*, 2018, **148**, 114104.

73 T. H. Dunning, *J. Chem. Phys.*, 1989, **90**, 1007–1023.

74 D. E. Woon and T. H. Dunning, *J. Chem. Phys.*, 1993, **98**, 1358–1371.

75 A. K. Wilson, T. van Mourik and T. H. Dunning, *J. Mol. Struct.*, 1996, **388**, 339–349.

76 S. Boys and F. Bernardi, *Mol. Phys.*, 1970, **19**, 553–566.

77 C. Schwartz, *Phys. Rev.*, 1962, **126**, 1015–1019.

78 J. Tennyson, M. Kostin, P. Barletta, G. Harris, O. Polyansky, J. Ramanlal and N. Zobov, *Comput. Phys. Commun.*, 2004, **163**, 85–116.

79 Atomic Weights and Isotopic Compositions with Relative Atomic Masses, 2005.

80 M. Beyer, A. Lammers, E. V. Savchenko, G. Niedner-Schatteburg and V. E. Bondybey, *Phys. Chem. Chem. Phys.*, 1999, **1**, 2213–2221.

This journal is © the Owner Societies 2024

Phys. Chem. Chem. Phys., 2024, **26**, 7060–7071 | **7071**